



ELSEVIER

Contents lists available at SciVerse ScienceDirect

Journal of Power Sources

journal homepage: www.elsevier.com/locate/jpowsour



Short communication

Synthesis and electrochemical performance of spinel-type LiMn_2O_4 using $\gamma\text{-MnOOH}$ rods as self-template for lithium ion battery

Lei He, Shichao Zhang*, Xin Wei, Zhijia Du, Guanrao Liu, Yalan Xing

School of Materials Science and Engineering, Beihang University, XueYuan Road No. 37, HaiDian District, Beijing 100191, PR China

HIGHLIGHTS

- The single crystalline LiMn_2O_4 rods obtained using $\gamma\text{-MnOOH}$ as a self-template.
- $\text{LiMn}_2\text{O}_4\text{-}450$ sample exhibits a high initial discharge capacity of $123.2 \text{ mA h g}^{-1}$ at 0.1C .
- $\text{LiMn}_2\text{O}_4\text{-}450$ sample maintains 84.0 mA h g^{-1} after 500 cycles at 10C .
- At 40C , $\text{LiMn}_2\text{O}_4\text{-}450$ sample presents a good discharge capability of 95.2 mA h g^{-1} .

ARTICLE INFO

Article history:

Received 30 May 2012

Received in revised form

29 July 2012

Accepted 31 July 2012

Available online 9 August 2012

Keywords:

Lithium-ion batteries

Lithium manganese oxide

High rate

Electrochemical performance

ABSTRACT

The single crystalline LiMn_2O_4 rods are synthesized by solid state reaction at varying temperatures (450°C and 550°C) using $\gamma\text{-MnOOH}$ rods as self-templates, which are obtained by a typical hydrothermal process. X-ray diffraction, scanning electron microscopy, transmission electron microscopy and electrochemical tests are thoroughly conducted/Performed to investigate its structure and properties. XRD, SEM and TEM observations show that LiMn_2O_4 spinel-type powders have good crystallinity and similar rods morphology with the width of $300\text{--}400 \text{ nm}$ and the length of $500 \text{ nm}\text{--}5 \text{ }\mu\text{m}$. As the cathode material for lithium batteries, LiMn_2O_4 synthesized at 450°C delivers higher initial discharge capacity of $123.2 \text{ mA h g}^{-1}$ at 0.1C and retains 84.0 mA h g^{-1} after 500 cycles at 10C rate. Even at a high current density of 40C , the material still presents an excellent discharge capability of 95.2 mA h g^{-1} . The probable effect of structure and prepared-temperature is analyzed in detail.

© 2012 Elsevier B.V. All rights reserved.

1. Introduction

In current years, lithium-ion batteries (LIBs) are widely used in portable electronic and have received much attention as a power source for hybrid electric vehicles and electric vehicles [1–3]. Spinel-type LiMn_2O_4 has been extensively studied as one of the most promising cathode materials for LIBs because of its intrinsic low-cost, environmental friendliness, high abundance, better safety and facile production [4,5]. However, it is difficult to meet the increasing requirement of high-power applications owing to the kinetic problems of the material, namely, a large polarization at high charge–discharge rates for the sluggish Li^+ ions diffusion in the solid active material [6–8].

Recently nanostructured lithium intercalated compounds with various morphologies have been extensively investigated to improve their rate capability by generating the favorable plane of

Li^+ ions diffusion: for instance, nanoparticles, nanowires, nanotubes, hollow spheres and mesoporous materials [9–12] and so on. However, such an improvement is often considered to be achieved at the expense of high volumetric energy density, which is incompatible with high power. As a consequence, a number of soft chemistry techniques to prepare LiMn_2O_4 have been explored to solve this problem, such as sol–gel method [13], Pechini process [14], combustion [15] and chemical precipitation [16]. Although uniform LiMn_2O_4 particles with good electrochemical performance could be thus obtained, the synthetic procedures are generally complex and costly. Therefore, solid state reaction route is highly recommended to synthesize high power capable nanosized materials, because it is simple and scalable.

Herein, $\gamma\text{-MnOOH}$ with a particular one-dimensional structure was considered as a possible precursor to produce nanosized LiMn_2O_4 electrode materials. But the greatest challenge is how to control the grain size distribution of the lithiated phase and maintain the nanorod morphology of $\gamma\text{-MnOOH}$ precursor during phase transformation. Reports have shown that chemical lithiation

* Corresponding author. Tel.: +86 10 82338148; fax: +86 10 82339319.

E-mail address: csc@buaa.edu.cn (S. Zhang).

of transition metal oxides could be a feasible method to enhance the performance of a Li-ion battery without significant change of oxide morphology [17,18]. In this paper, we successfully synthesized spinel-type LiMn_2O_4 rods via a facile two-step process: a hydrothermal reaction to prepare $\gamma\text{-MnOOH}$ rods and the following solid state reaction with LiOH . To understand the rate capability of the LiMn_2O_4 synthesized at various temperatures, structure and morphology were investigated and the probable mechanism was also discussed.

2. Experimental

The synthesis of $\gamma\text{-MnOOH}$ was carried out via one-step hydrothermal method. The stoichiometric amount of $\text{MnSO}_4 \cdot \text{H}_2\text{O}$, KMnO_4 and CTAB (Hexadecyl trimethyl ammonium bromide) was mixed well in distilled water and stirred for an hour. Afterward, the suspension was transferred into a 100 mL Teflon-lined stainless-steel autoclave, sealed and maintained at 160 °C for 25 h. The product was cooled to room temperature, filtered and washed with distilled water, ethanol and acetone. Finally, the brown powder were obtained and dried under vacuum at 60 °C for 10 h.

LiMn_2O_4 powder was prepared by the following procedure: A stoichiometrically required amount of as-prepared $\gamma\text{-MnOOH}$ was added to an aqueous solution of $\text{LiOH} \cdot \text{H}_2\text{O}$ and stirred for an hour. The mixture was dried in a vacuum oven/oven, and then the solid product was ground and calcined in air at 450 °C and 550 °C for 15 h, respectively. The final products were referred to as “ $\text{LiMn}_2\text{O}_4\text{-450}$ ” and “ $\text{LiMn}_2\text{O}_4\text{-550}$ ”, respectively.

X-ray diffraction (XRD, Rigaku D/Max-2400, Japan) using $\text{Cu K}\alpha$ radiation was employed to identify the crystalline phase of the synthesized material. The data were recorded in the 10–80° 2θ range at the scanning rate of 6° min⁻¹. The patterns were analyzed by the Rietveld method as implemented in the program GSAS. Scanning electron microscopy (SEM, Hitachi S-4800, Japan), transmission electron microscopy (TEM) and high-resolution transmission electron microscopy (HR-TEM, JEOL-2100F, Japan) were engaged to observe morphology, size and distribution of as-prepared compounds. X-ray photoelectron spectroscopy (XPS) was collected using American PHI5700ESCA with a non-monochromatic $\text{Mg K}\alpha$ (1253.6 eV) light source.

The electrodes were fabricated by casting a slurry of 75 wt.% active material, 15 wt.% carbon black, and 10 wt.% poly(vinylidene fluoride) (PVDF) in *N*-methylpyrrolidinone (NMP) solvent onto an Al foil substrate. The slurry was dried in vacuum at 60 °C overnight. The film was cut into pieces of about 0.6 × 0.6 cm² to act as electrodes. The testing half-cells were assembled in an Ar-filled glove box (MB-10-G with TP170b/mono, MBRAUN) with lithium metal as counter and reference electrode. Electrolyte was 1 M LiPF_6 in a mixed solution of EC and DEC (1:1 in volume ratio). The charge–discharge measurements were galvanostatically carried out using a battery test system (NEWARE BTS-610, Newware Technology Co., Ltd., China) at different current densities in the voltage range of 2.0–4.6 V (vs. Li/Li^+). Cyclic voltammograms (CVs) were measured with an electrochemical workstation (CHI1100A) at a scan rate of 0.1 mV s⁻¹ between 3.3 and 4.5 V (vs. Li/Li^+).

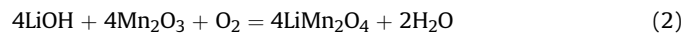
3. Results and discussion

3.1. The evolution of MnOOH to LiMn_2O_4 and the characterization of LiMn_2O_4

Fig. 1 shows the Rietveld refinement of XRD pattern, SEM and TEM images of the nanostructured $\gamma\text{-MnOOH}$. All the peaks in the Fig. 1a can be indexed to a monoclinic phase (JCPDS No. 41-1379) with lattice constants $a = 5.300\text{\AA}$, $b = 5.278\text{\AA}$ and $c = 5.307\text{\AA}$. Fig. 1b

shows the SEM image of as-prepared $\gamma\text{-MnOOH}$ rods. It is observed that a large quantity of uniform rod-like nanostructures were formed with about 200–300 nm in width and approximately 8 μm in length. The rod-like nanostructure of the sample is further examined by TEM and HRTEM as shown in Fig. 1c–e. The result demonstrates its single-crystalline structure corresponding to the selected area electron diffraction (SAED) pattern (Fig. 1d). The diffraction spots can be indexed to (111), (020) and (131) planes of monoclinic $\gamma\text{-MnOOH}$ (JCPDS No. 41-1379). The HRTEM image (Fig. 1e) corresponding to the circled area marked in Fig. 1c indicates clearly the atom arrangements, which further confirms the single-crystalline structure of $\gamma\text{-MnOOH}$. As depicted in Fig. 1e, interplanar spacings of (020) and (111) is 2.6 Å and 3.4 Å, respectively.

Fig. 2 shows XRD patterns and the Rietveld refinement profiles of the LiMn_2O_4 precursors calcined at varying temperatures for 15 h in air. All the peaks can be indexed to a pure cubic spinel phase ($\text{Fd}3\text{m}$, space group 227) which corresponds to JCPDS data No.35-0782, shown in Fig. 2a. Small quantities of Mn_2O_3 were detected in $\text{LiMn}_2\text{O}_4\text{-450}$ sample which were not in $\text{LiMn}_2\text{O}_4\text{-550}$ sample. The characteristic peaks of two samples are similar, whereas the peak intensity is increased with the ascent of synthesis temperature. The result implies that the crystallinity of $\text{LiMn}_2\text{O}_4\text{-450}$ sample is lower while that of $\text{LiMn}_2\text{O}_4\text{-550}$ is higher. The data for the samples obtained at 450 °C and 550 °C were listed in Table 1. Two samples have slight difference in cell parameters, indicating their similar structure. The position and full width at half maximum (FWHM) of the (311)-plane peak are the important factors for the crystallinity of spinel structure, as reported by Manev et al. [19] and Lee et al. [20]. The data in Table 1 displays that $\text{LiMn}_2\text{O}_4\text{-550}$ owns higher crystallinity than $\text{LiMn}_2\text{O}_4\text{-450}$, consistent with results in Fig. 2a. On the other hand, the lattice parameter value of the $\text{LiMn}_2\text{O}_4\text{-450}$ is the closed to the critical lattice parameter values of 8.23 Å [21]. The synthesis procedure could be described as follows:



X-ray photoelectron spectroscopy (XPS) has been widely used to study the electronic structure of materials. The XPS binding energies provide chemical information such as the oxidation state. The Mn 2p XPS spectra of LiMn_2O_4 sintered at different temperatures are shown in Fig. 3. The Mn 2p_{3/2} binding energies of the samples with the sintering temperature of 450 °C and 550 °C are found to be 642.4 eV and 642.5 eV, respectively, indicating that the Mn oxidation state in spinel-type LiMn_2O_4 was almost the same between +3 and +4 [22]. However, in the XRD results, the small amounts of impure phases presented at 450 °C can be identified as Mn_2O_3 . Therefore, due to the Mn^{3+} existed in Mn_2O_3 at 450 °C which was not shown at 550 °C, the proportion of Mn^{4+} atoms is larger in samples at 450 °C than that at 550 °C. These results are in agreement with the XRD analysis above. Hence, we think that the synthesis temperature 450 °C is suitable for the high performance of lithium ion batteries as follows.

LiMn_2O_4 has a three-dimensional lithium diffusion path and every plane is suitable to exchange lithium ion from active materials to the electrolyte, attribute to favorable spinel cubic structure [23]. Fig. 4 shows the SEM, TEM, HRTEM and SAED images of LiMn_2O_4 rods obtained at varying temperatures. The SEM images (Fig. 4a and b) show that two samples have similar rods morphology with the width of 300–400 nm and the length of 500 nm–5 μm . Slight agglomeration can be observed with the increasing of temperature. All the samples were well dispersed and maintained the morphology of $\gamma\text{-MnOOH}$ rods self-template after

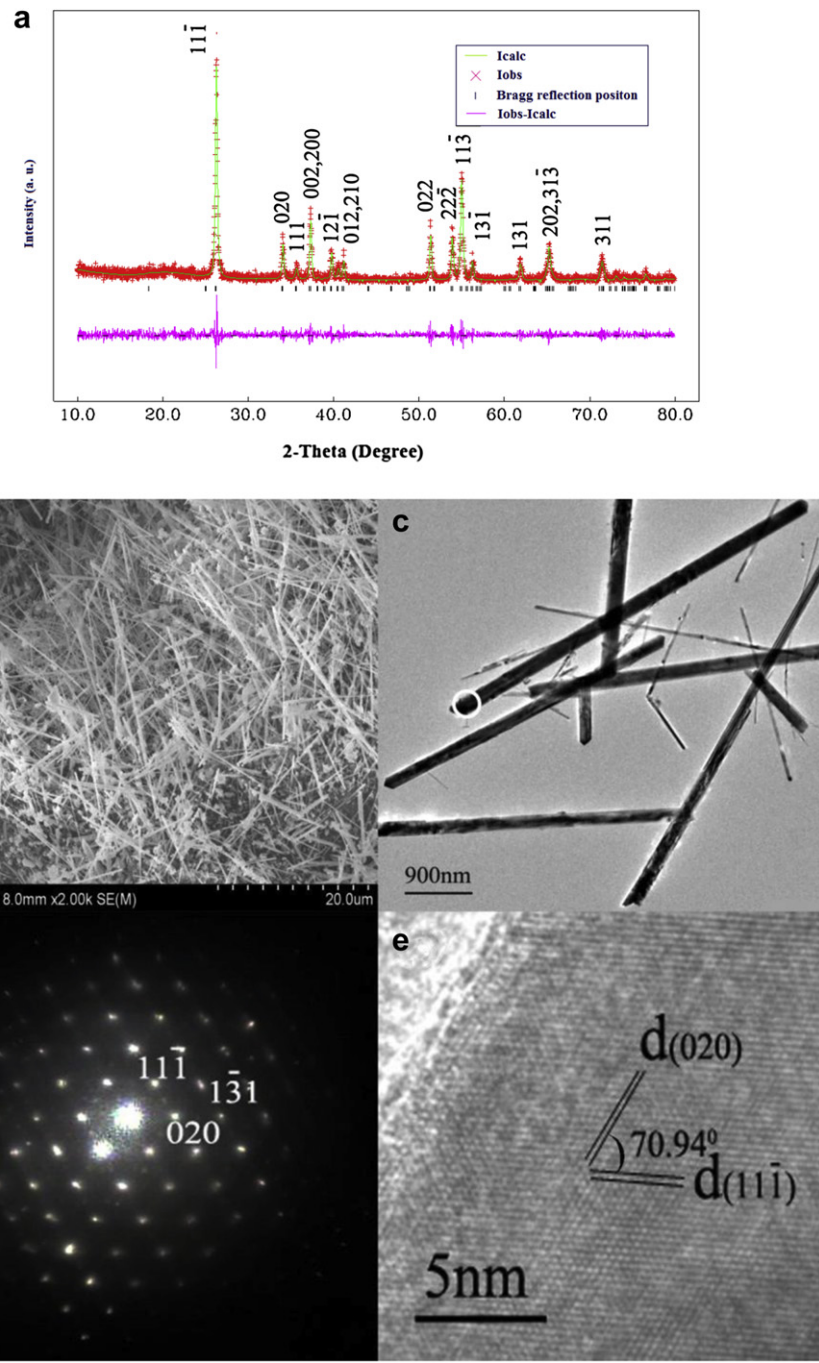


Fig. 1. (a) Rietveld refinement of XRD pattern of γ -MnOOH rods; (b) SEM, (c) TEM, (d) corresponding SAED patterns and (e) HR-TEM images of γ -MnOOH rods.

an irreversible phase transition, only that rods became shorter in length [23]. It is probably ascribed to the high-temperature process/damage. Generally/However, it is favorable to shorten the path of intercalation/deintercalation for lithium ion to some extent, thus increasing the actual specific capacity. Rod-like nanostructure of the samples was further examined by TEM and HR-TEM. The HR-TEM images (Fig. 4c and d) show that all the samples are single crystalline and consist with cubic structure. The diffraction spots (Fig. 4e and f) can be indexed to (220) and (311) planes of cubic spinel-type LiMn_2O_4 (JCPDS data No.35-0782). With an increased calcining temperature, the primary width of the LiMn_2O_4 rods rises, the appearance of the primary rods becomes breakdown, and the amount of big particles increases.

3.2. The electrochemical reaction mechanism of LiMn_2O_4

Cyclic voltammograms test was engaged to analyze oxidation/reduction and phase transformation processes in electrode reactions [24–26]. Fig. 5 depicts the CV curves measured in the potential range of 3.3–4.5 V at a sweep rate of 0.1 mV s^{-1} . The CV curves exhibit two pairs of clearly separated oxidation/reduction peaks. The higher oxidation/reduction peaks attribute to Li^+ intercalation/deintercalation from the 8a sites where $\text{Li}-\text{Li}$ interactions do not occur, corresponding to Li^+ intercalation/deintercalation over the x value range of $0 \leq x \leq 0.5$ in $\text{Li}_x\text{Mn}_2\text{O}_4$. The lower ones are owing to Li^+ intercalation/deintercalation from the 8a sites but where $\text{Li}-\text{Li}$ interactions occur, corresponding to Li^+

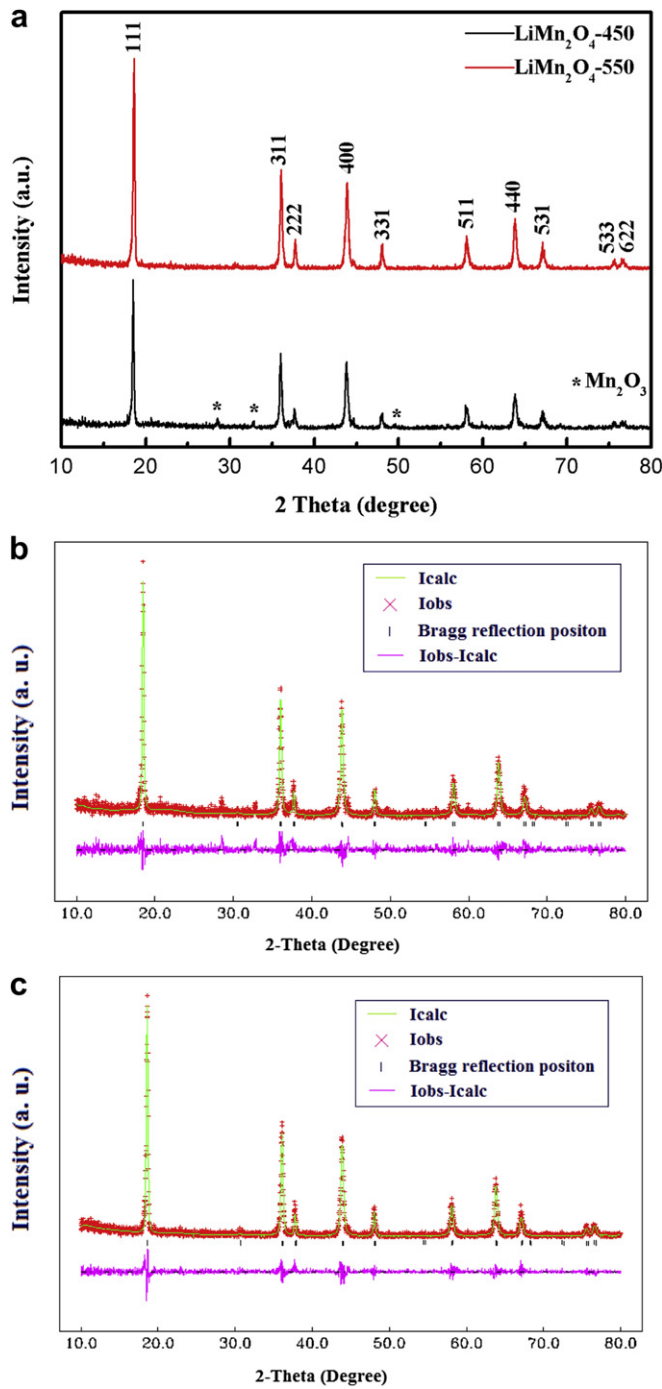


Fig. 2. (a) XRD patterns for the LiMn_2O_4 precursors calcined at various temperatures and Rietveld refinement for XRD patterns of the LiMn_2O_4 precursors calcined at varying temperatures: (b) 450 °C; (c) 550 °C.

Table 1

Cell parameters data for the cubic spinel-type LiMn_2O_4 samples obtained at different temperatures.

Sample	LiMn_2O_4 -450	LiMn_2O_4 -550
a (Å)	8.228	8.243
V (Å ³)	557.087	560.285
Plane (311)/degree	36.02	36.08
Position/2θ	0.33	0.30

intercalation/deintercalation over the x value range of $0.5 \leq x \leq 1$ in $\text{Li}_x\text{Mn}_2\text{O}_4$ [27]. LiMn_2O_4 -450 sample exhibits higher peak current and peak area, shown in Fig. 5(a). It indicates higher discharge capacity, consistent with the results discussed above. While LiMn_2O_4 -550 sample shows a lower one (Fig. 5(b)). The reason may be that stoichiometric LiMn_2O_4 begins to lose oxygen and disproportionates to rocksalt phase LiMnO_2 and tetragonal $\text{Li}_{1-2x}\text{Mn}_{2-x}\text{O}_{4-2x-y}$ when heated approximately 550 °C [28]. Table 2 shows the experimental data of the ratio of peak currents (I_{pa}/I_{pc}) and potential interval between oxidation peak and reduction peak ($\Delta\phi_p$). The experimental data of I_{pa}/I_{pc} and $\Delta\phi_p$ for the LiMn_2O_4 -450 sample respectively are 1.04 and 127 mV, however, those for the LiMn_2O_4 -550 sample are 1.08 and 140 mV. It demonstrates that lithium ions are intercalated and deintercalated reversibly in the LiMn_2O_4 samples obtained at low temperature, just as reported [29].

Fig. 6 shows the initial charge–discharge curves of the sample LiMn_2O_4 -450 and LiMn_2O_4 -550 at 0.1C (1C = 148 mA h g⁻¹). All the samples exhibit two plateaus around 3.95 and 4.18 V, due to two-step oxidation/reduction process of spinel-type LiMn_2O_4 [23,30], consistent well with the results shown in Fig. 5. The initial charge and discharge specific capacity of LiMn_2O_4 -450 sample are 148.0 mA h g⁻¹ and 131.5 mA h g⁻¹ respectively, with a columbic efficiency of 88.9%. The initial charge and discharge specific capacity of LiMn_2O_4 -550 sample are 142.7 and 129.4 mA h g⁻¹ respectively, exhibiting a little higher columbic efficiency of 90.7%. However, it is obvious that LiMn_2O_4 -550 exhibits much narrower potential plateaus than LiMn_2O_4 -450. It is probably owing to the agglomeration of the grains caused by the sintering process at much higher temperature. It probably reduces specific surface area of the sample and blocks the full penetration of electrolyte, and thereby cuts down the quantity of intercalation/deintercalation for lithium ion.

3.3. The rate capability and cycling performance of LiMn_2O_4

Rate performance was investigated at the varying rate from 0.1C (14.8 mA g⁻¹) to 40C (5920 mA g⁻¹) in the first discharge cycle. As shown in Fig. 7a, the discharge specific capacities of LiMn_2O_4 -450 are 131.5 mA h g⁻¹, 128.7 mA h g⁻¹, 127.6 mA h g⁻¹, 127.4 mA h g⁻¹, 112.2 mA h g⁻¹, 103.7 mA h g⁻¹ and 95.2 mA h g⁻¹, corresponding the current rate of 0.1C, 1C, 2C, 3C, 10C, 20C and 40C, respectively.

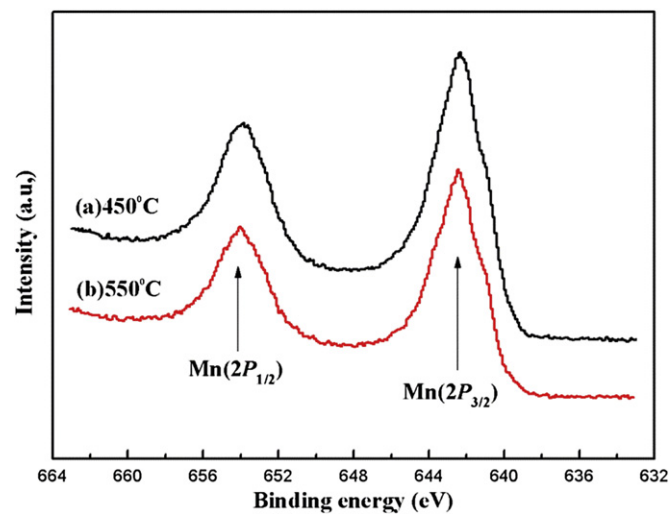


Fig. 3. Mn 2p XPS spectrum of the spinel-type LiMn_2O_4 sintered different temperatures: (a) 450 °C and (b) 550 °C.

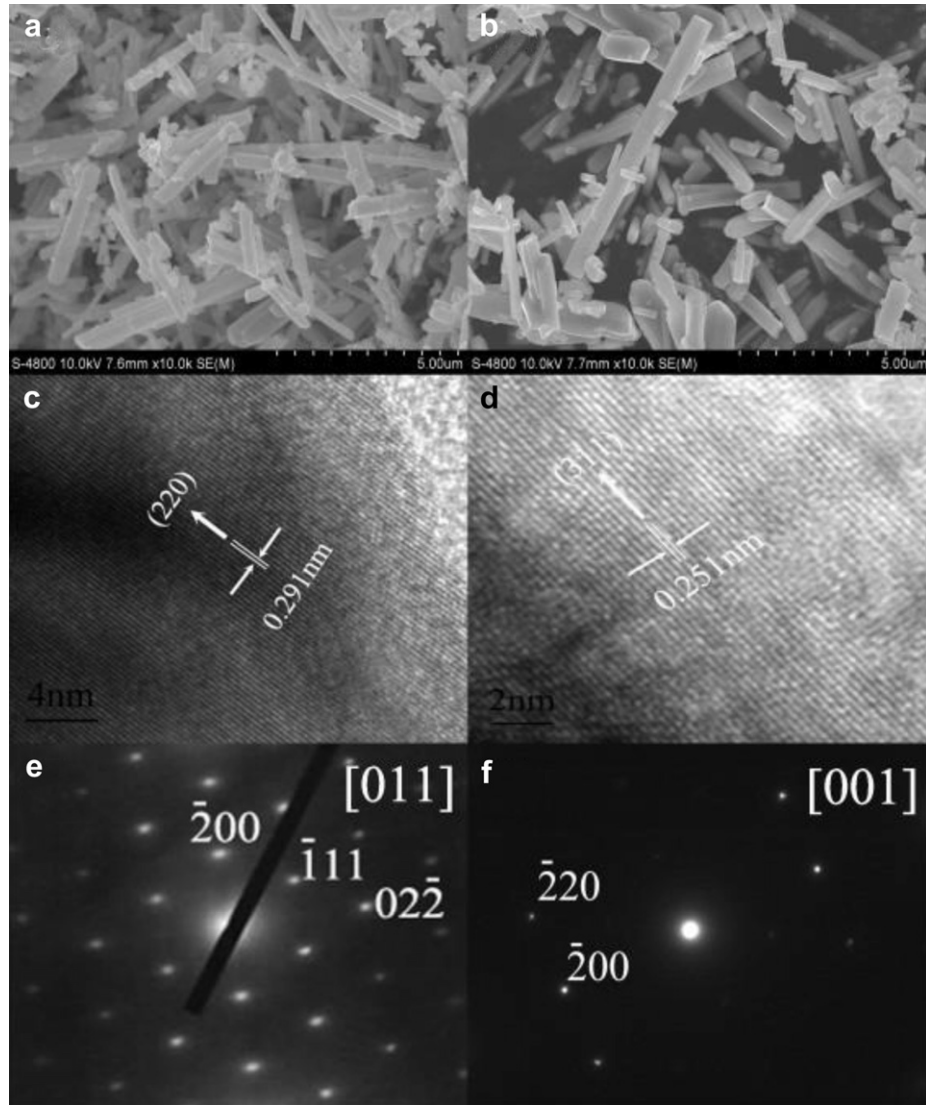


Fig. 4. SEM, TEM, HRTEM and SAED images of LiMn_2O_4 rods obtained at varying temperatures: (a, c, e) LiMn_2O_4 -450; (b, d, f) LiMn_2O_4 -550.

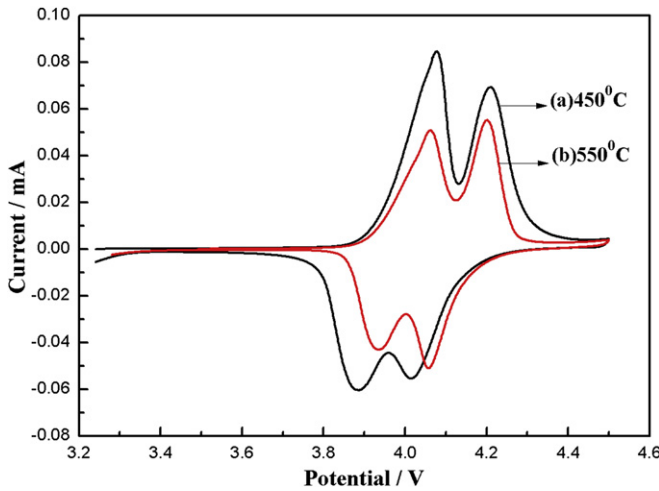


Fig. 5. Cyclic voltammograms curves of the LiMn_2O_4 -450 and LiMn_2O_4 -550 samples.

While discharge capacity of the LiMn_2O_4 -550 rods cathode decreases to $129.4 \text{ mA h g}^{-1}$, 122 mA h g^{-1} , 119 mA h g^{-1} , $112.7 \text{ mA h g}^{-1}$, $109.4 \text{ mA h g}^{-1}$, 99.3 mA h g^{-1} and 92.6 mA h g^{-1} , corresponding the current rate of 0.1C, 1C, 2C, 3C, 10C, 20C and 40C, respectively. Under the same rate, the discharge capacity of LiMn_2O_4 -450 sample is higher than that of LiMn_2O_4 -550. As the current rate increases, the pseudo plateau of discharge curve for the two samples moved downward. In fact, at lower rates the cell operates/react close to equilibrium conditions, whereas at higher rates electrode overpotentials and the internal resistant drop, mainly due to the low conductive organic electrolyte increase, thus decreasing the operating voltage of the cell [31]. Even at 40C, the LiMn_2O_4 -450 sample still has a flat voltage plateau about 3.75 V and

Table 2

The experimental data of the ratio of peak currents (I_{pa}/I_{pc}) and potential interval between oxidation peak and reduction peak ($\Delta\phi_p$).

Samples	ϕ_{pa} (V)	ϕ_{pc} (V)	$\Delta\phi_p$ (mV)	I_{pa} (mA)	I_{pc} (mA)	I_{pa}/I_{pc}
LiMn_2O_4 -450	4.188	4.061	127	0.0750	0.0715	1.04
LiMn_2O_4 -550	4.200	4.06	140	0.0553	0.0510	1.08

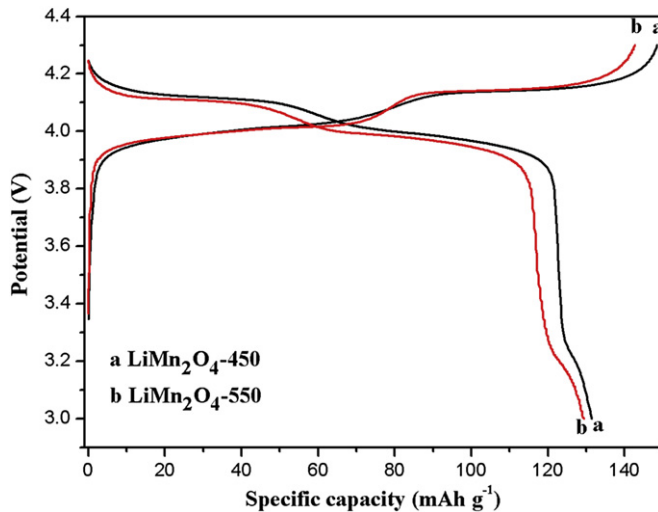


Fig. 6. Initial charge–discharge curves of LiMn_2O_4 -450 and LiMn_2O_4 -550 samples in the range of 3.0–4.3 V (vs. Li/Li^+) at 0.1C.

delivers 95.2 mA h g^{-1} . The results show that this kind of cathode material has good rate performance and low polarization.

Fig. 8a shows the cycling stability curves for LiMn_2O_4 -450 and LiMn_2O_4 -550 samples at varying rates in the potential range of

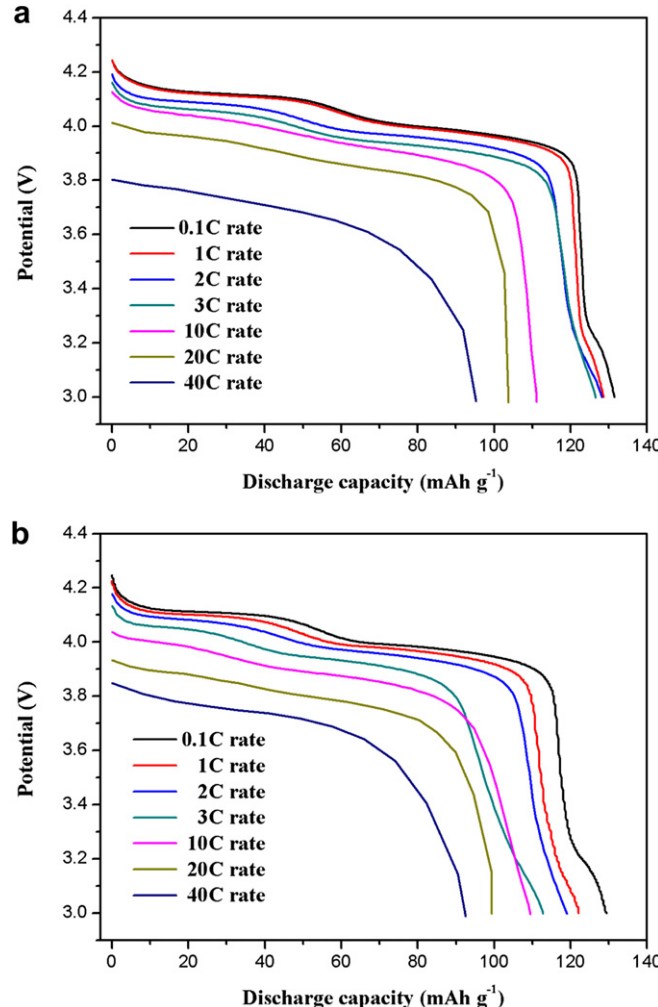


Fig. 7. The initial discharge curves of LiMn_2O_4 -450 (a) and LiMn_2O_4 -550 (b) at different current densities.

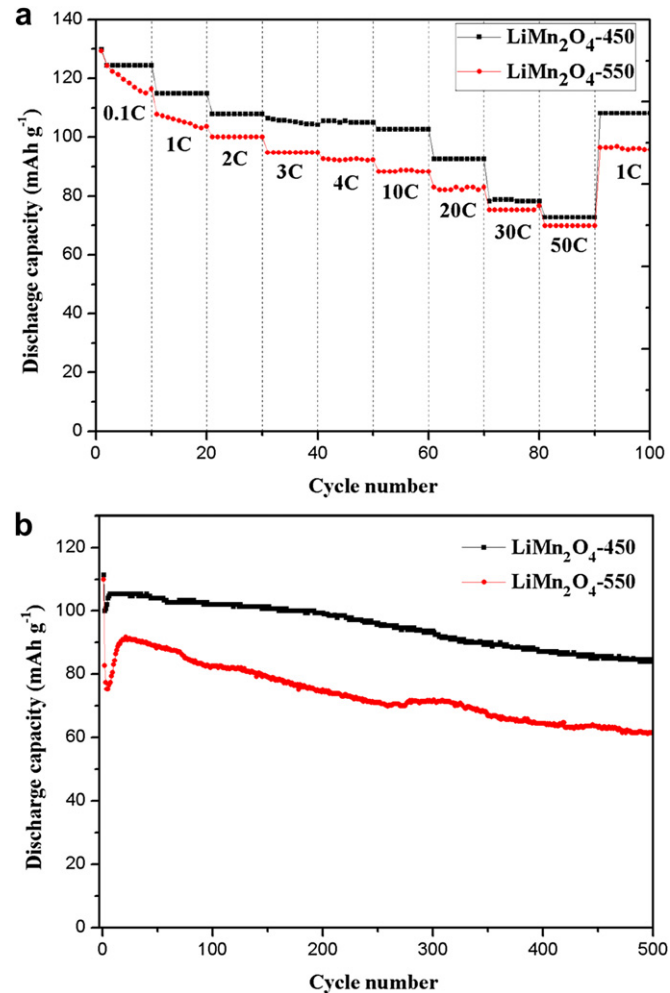


Fig. 8. (a) Cycling stability curves of LiMn_2O_4 -450 and LiMn_2O_4 -550 samples at varying rates in the potential range of 3.0–4.3 V; (b) cycling stability of LiMn_2O_4 -450 and LiMn_2O_4 -550 at a 4C rate in the potential range of 3.0–4.3 V.

3.0–4.3 V. The discharge capacity of the LiMn_2O_4 -450 sample is higher than that of LiMn_2O_4 -550 sample at the same rates. The discharge capacity of the LiMn_2O_4 -450 sample remains stable and decreases regularly and steadily as the rate increases. Moreover, the capacity can be approximately recovered to the initial value when the current density is raised to 1C rate again. It implies that both of the two samples own good electrochemical reversibility and cycle stability, in which LiMn_2O_4 -450 sample is better. Fig. 8b shows the cycling stability of LiMn_2O_4 -450 and LiMn_2O_4 -550 at a 10C rate in the potential range of 3.0–4.3 V. The initial irreversible capacity loss of LiMn_2O_4 -450 and LiMn_2O_4 -550 are 10.1% and 24.7%, respectively, caused by the formation of solid electrolyte interphase (SEI) layer [32]. After the first cycle, the LiMn_2O_4 -450 sample exhibits excellent cycling performance. It shows a quite slow capacity fading with an average capacity loss of 0.03 mA h g^{-1} per cycle during 500 charge–discharge cycles, in other words, the discharge capacity of LiMn_2O_4 -450 maintains above 85% of its second capacity after 500 cycles, whereas capacity retention is 74.4% for the LiMn_2O_4 -550 electrode.

3.4. The morphology maintenance of LiMn_2O_4 during cycling

Furthermore, to better understand the merits of the rod- LiMn_2O_4 during cycling, the electrode fabricated from the cathode active

materials of LiMn₂O₄-450 observed before and after 300, 500 cycles at 10C-rate with SEM. Fig. 9(a) is a SEM image showing the surface of the single crystalline LiMn₂O₄ electrode before cycle, where the integrity of electrode can be clearly observed. Then after 300 cycles, the surface of electrode almost has no change in Fig. 9(b). After 500 cycles, some cracks of rods can be clearly observed on the surface of the electrode, however, where the integrity and the uniform rods of the electrode are retained shown in Fig. 9(c). It is well-known that Li

ions can be intercalated in the empty octahedral sites of the LiMn₂O₄ spinel structure to form Li_{1+x}Mn₂O₄. In addition, the irreversible variations of spinel cubic structure in the cycling existed for the LiMn₂O₄ material, and those variations can be speculated due to Jahn–Teller effect. Besides, LiMn₂O₄ has a three-dimensional lithium diffusion path due to favorable spinel cubic structure. Every plane is suitable to exchange lithium ion from active materials to the electrolyte. Therefore, the very good performances of submicron rod-LiMn₂O₄ synthesized at 450 °C can be understood in terms of morphological and structural features.

4. Conclusions

The single crystalline LiMn₂O₄ rods have been successfully prepared by solid state reaction using γ-MnOOH rods as a self-template. Synthesized temperature has great influence in electrochemical performance of single crystalline LiMn₂O₄ cathode materials. The results show that LiMn₂O₄-450 sample has better discharge capacity, cycle stability and rate performance. It exhibits a high initial discharge capacity (111.3 mA h g⁻¹) at 10C, maintaining 84 mA h g⁻¹ after 500 cycles. Even at a high current density of 40C, the material still presents an excellent discharge capability of 95.2 mA h g⁻¹. It is meaningful to research high performance spinel-type LiMn₂O₄ as promising substitute of cathode materials for novel lithium ion battery in application.

Acknowledgments

This work was supported by the National Natural Science Foundation of China (Grants 50954005 and 51074011), the National 863 Program (Grants 2006AA03Z230 and 2008AA03Z208), and the National Basic Research Program of China (Grant 2007CB936502).

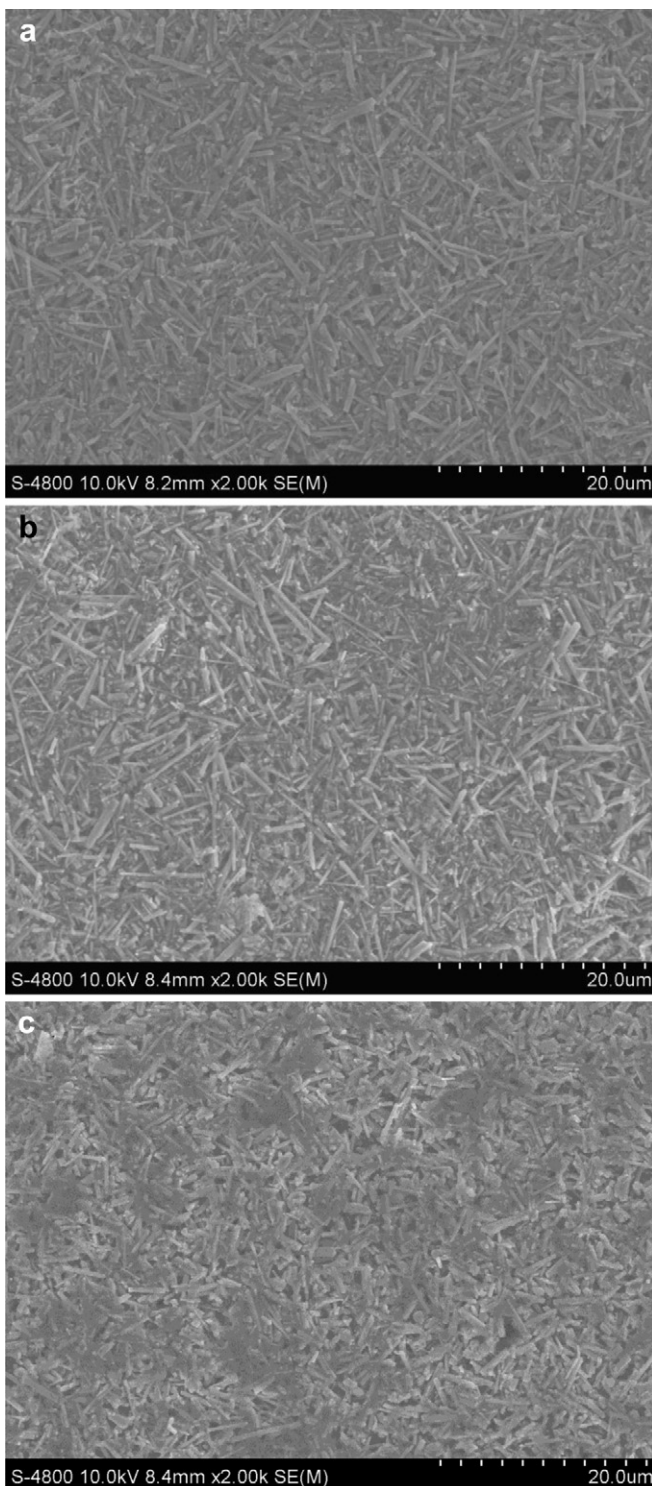
Appendix A. Supplementary material

Supplementary data related to this article can be found online at <http://dx.doi.org/10.1016/j.jpowsour.2012.07.118>.

References

- [1] J.M. Tarascon, M. Armand, *Nature* 414 (2001) 359–367.
- [2] M.S. Whittingham, *Chem. Rev.* 104 (2004) 4271–4301.
- [3] A.S. Arico, P. Bruce, B. Scrosati, J.M. Tarascon, W.V. Schalkwijk, *Nat. Mater.* 4 (2005) 366–377.
- [4] J.M. Tarascon, W.R. McKinnon, F. Coowar, T.N. Bowmer, G. Amatucci, D. Guyomard, *J. Electrochem. Soc.* 141 (1994) 1421–1431.
- [5] N.J. Dudney, J.B. Bates, R.A. Zuer, S. Young, J.D. Robertson, H.P. Jun, S.A. Hackney, *J. Electrochem. Soc.* 146 (1999) 2455–2464.
- [6] L.H. Yu, H.X. Yang, X.P. Ai, Y.L. Cao, *J. Phys. Chem. B* 109 (2005) 1148–1154.
- [7] F. Jiao, K.M. Shaju, P.G. Bruce, *Angew. Chem. Int. Ed.* 44 (2005) 6550–6553.
- [8] Y.G. Guo, Y.S. Hu, W. Sigle, J. Maier, *Adv. Mater.* 19 (2007) 2087–2091.
- [9] T. Doi, Y. Iriyama, T. Abe, Z. Ogumi, *Chem. Mater.* 17 (2005) 1580–1582.
- [10] E. Hosono, T. Kudo, I. Honma, H. Matsuda, H. Zhou, *Nano Lett.* 9 (2009) 1045–1051.
- [11] Y.L. Ding, J. Xie, G.S. Cao, T.J. Zhu, H.M. Yu, X.B. Zhao, *Adv. Funct. Mater.* 21 (2011) 348–355.
- [12] J.Y. Luo, H.M. Xiong, Y.Y. Xia, *J. Phys. Chem. C* 112 (2008) 12051–12057.
- [13] C.J. Curtis, J.X. Wang, D.L. Schulz, *J. Electrochem. Soc.* 151 (2004) 590–598.
- [14] S.H. Wu, H.L. Chen, *J. Power Sources* 119–121 (2003) 134–138.
- [15] K. Du, H. Zhang, *J. Alloys Compd.* 352 (2003) 250–254.
- [16] A.R. Naghash, J.Y. Lee, *J. Power Sources* 85 (2000) 284–293.
- [17] B. Garcia, M. Millet, J.P. Pereira-Ramos, N. Baffier, D. Bloch, *J. Power Sources* 81–82 (1999) 670–674.
- [18] L. Mai, B. Hu, W. Chen, Y. Qi, C. Lao, R. Yang, Y. Dai, Z.L. Wang, *Adv. Mater.* 19 (2007) 3712–3716.
- [19] V. Manev, T. Faulkner, J. Engel, in: Proc. HBC98, The First Hawaii Battery Conference, 1998, p. 228.
- [20] Y.S. Lee, N.J. Kumada, M. Yoshio, *J. Power Sources* 96 (2001) 376.
- [21] Fábio A. Amaral, Nerilso Bocchi, Ricardo F. Brocenschi, Sonia R. Biaggio, Romeu C. Rocha-Filho, *J. Power Sources* 195 (2010) 3293–3299.
- [22] K.M. Shaju, G.V. SubbaRao, B.V.R. Chowdari, *Solid State Ionics* 152–153 (2002) 69–81.

Fig. 9. SEM images of the LiMn₂O₄-450 electrode before and after 300, 500 cycles. (a) Before initial discharge. (b) After 300 cycles. (c) After 500 cycles.



- [23] H.-W. Lee, P. Muralidharan, R. Ruffo, C.M. Mari, Y. Cui, D.K. Kim, *Nano Lett.* 10 (2010) 3852–3856.
- [24] N. Ding, J. Xu, Y.X. Yao, G. Wegner, X. Fang, C.H. Chen, I. Lieberwirth, *Solid State Ionics* 180 (2009) 222–225.
- [25] S.B. Tang, M.O. Lai, L. Lu, *Mater. Chem. Phys.* 111 (2008) 149–153.
- [26] S.R. Das, S.B. Majumder, R.S. Katiyar, *J. Power Sources* 139 (2005) 261–268.
- [27] W. Liu, G.C. Farrington, F. Chaput, B. Dunn, *J. Electrochem. Soc.* 143 (1996) 879–892.
- [28] K. Miura, A. Yamada, M. Tanaka, *Electrochim. Acta* 41 (1996) 249–256.
- [29] Y.Y. Xia, H. Takeshige, H. Noguchi, M. Yoshio, *J. Power Sources* 56 (1995) 61–67.
- [30] D.K. Kim, P. Muralidharan, H.W. Lee, R. Ruffo, Y. Yang, C.K. Chan, H. Peng, R.A. Huggins, Y. Cui, *Nano Lett.* 8 (2008) 3948–3952.
- [31] D. Linden, T.B. Reddy, *Handbook of Batteries*, third ed., McGraw-Hill, New York, 2002, pp. 2.1–2.37.
- [32] Y.G. Guo, J.S. Hu, L.J. Wan, *Adv. Mater.* 20 (2008) 2878–2887.